Design of a freeform, dual fields-of-view, dual focal lengths, off-axis three-mirror imaging system with a point-by-point construction-iteration process

Tong Yang (杨 通), Jun Zhu (朱 钧)*, and Guofan Jin (金国藩)

State Key Laboratory of Precision Measurement Technology and Instruments, Department of Precision Instrument, Tsinghua University, Beijing 100084, China

**Corresponding author: j_zhu@tsingua.edu.cn*

Received June 14, 2016; accepted August 26, 2016; posted online September 30, 2016

In this Letter, we propose a novel configuration and design method of freeform, dual fields-of-view (FOVs), dual focal lengths, off-axis three-mirror zoom imaging systems. The switch of the two zooms is achieved by rotating a single mirror element. The design of a freeform, dual focal lengths zoom system is realized by a point-by-point design approach for the first time to our knowledge. This method enables the direct design of freeform surfaces from initial planes using given system specifications and configuration, and the designed system can be taken as a good starting point for further optimization. A freeform, dual FOVs, dual focal lengths, off-axis three-mirror zoom system is demonstrated. The F-numbers of the two zooms are 2 and 2.4. The dual FOVs are $3° \times 3°$ and $2.5° \times 2.5°$. After final optimization, both of the zooms achieve high performances.

OCIS codes: 080.4228, 080.4035, 220.2740.

doi: 10.3788/COL201614.100801.

The zoom optical system is a kind of system with important functions[1,2]. The effective focal length (EFL) of the zoom system is variable. Among the different kinds of zoom systems, the non-continuous zoom system with double EFLs and dual fields of view (FOVs) is a special and useful case. These optical systems have a short-focus zoom with a wider FOV and a long-focus zoom with a narrower FOV. Up to now, most of the dual FOVs, dual EFLs systems have been refractive systems[3–6]. However, refractive systems have the shortcomings of heavy weight, low transmission, radiation sensitivity, high chromatic aberrations, and thermal instability, etc. Reflective system configurations can be used to overcome these shortcomings, as they have the advantages of light weight, high transmission, radiation resistance, absence of chromatic aberrations, and thermal stability[7–9]. However, the central obscuration in traditional coaxial reflective systems greatly limits the resolution, energy concentration, and FOV. So the unobscured, off-axis reflective system is a better choice[10]. But the unconventional aberrations induced by the non-symmetric configurations will make the design extremely difficult, as they can be hardly corrected by traditional spherical or aspherical surfaces.

A method for getting a higher performance while operating off-axis is to use freeform surfaces[11]. They are defined as non-rotationally symmetric surfaces and offer more degrees of design freedom in the optical design[12]. Traditional freeform system design for imaging optics is based on optimization from a starting point (which is generally found from existing patents or systems). But for unobscured reflective zoom system design, there are few proper starting points to choose from. So, designers may have to find some other systems as the starting points, whose configuration, number of elements, and system specifications (such as FOV, F-number, and focal length) are generally far from the expected specifications of the current design. In this way, the design of the system will be very difficult. Designers may fail to find useful solutions, or they may have to spend a very long time improving the starting point. Direct design methods of freeform surfaces provide promising ways to generate a good starting point for the subsequent design. The partial differential equations (PDEs) method[13–15], the simultaneous multiple surface (SMS) design method[16], as well as a related analytic design method[17], and a newly proposed two-surface freeform lens design method[18] are typical direct design methods of freeform optics. But none of these methods can achieve the design of a dual-FOVs zoom system. Recently, the construction-iteration (CI) method has been proposed[19]. This method uses the light rays from multiple fields and different pupil coordinates in a point-by-point direct design process. However, this method cannot design dual-EFLs zoom systems either. The direct design of freeform, dual-EFLs zoom systems remains a big challenge.

In this Letter, we propose a novel configuration to realize freeform, dual-FOVs, dual-EFLs, three-mirror zoom systems. Among all the surfaces in the system, only one surface is different in two zooms. Other surfaces, including the image plane, remain the same and fixed. Here, the secondary mirror (M2) is chosen to be different in two zooms, as shown in Fig. 1. The two different surfaces corresponding to the two zooms can be fabricated directly on the two opposite sides of one element, or they are fabricated individually and then mounted onto the two opposite sides of one element. The switch of the zooms (dual FOVs) is

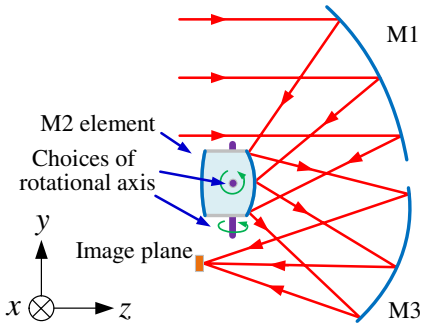

Fig. 1. Configuration of the freeform, dual-FOVs, dual-EFLs, off-axis, three-mirror zoom system.

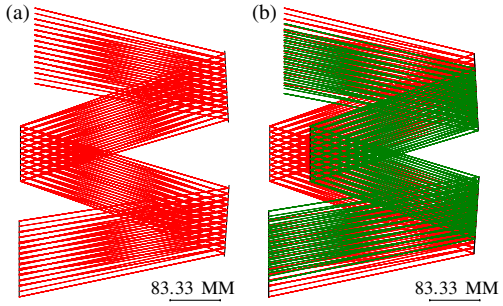

Fig. 2. Layout of the initial planar system. (a) The system for the short-focus zoom. (b) The initial planar system for the long-focus zoom can be obtained after calculating Δ. The two zooms are overlaid in this figure. The red and green rays represent the rays in the short- and long-focus zooms, respectively.

achieved by rotating the M2 element along a rotational axis in the x direction or y direction. The primary mirror (M1), the tertiary mirror (M3), and the image plane are fixed in the system during the switch of the zooms.

A design method of this kind of zoom system has been proposed. This is, to the best of the authors' knowledge, the first time the design of a dual focal lengths zoom system has been realized by a point-by-point design approach. The design is based on the point-by-point CI process. A freeform, off-axis, three-mirror, dual-FOVs zoom system is demonstrated. The system specifications are listed in Table 1.

An initial system with three decentered and tilted planes for the first zoom (here we choose the short-focus zoom) is first established for the subsequent design process, as shown in Fig. 2(a). The initial planes are located approximately at the places where the final freeform surfaces are expected to be. M2 is taken as the aperture stop. The initial system for the long-focus zoom is established later. The two zooms use biased a FOV in the y direction with the same central field (0°, –12°). When designing non-rotationally symmetric freeform surfaces, feature rays over the entire aperture and FOV must be used. The number of feature rays should not be too small in order to better characterize the shape of the surface and get high accuracy. In addition, to avoid a long computation time, the number of rays should not be too large. Here, six sample fields over the half-full FOV were employed for each zoom in the surface construction process. For the short-focus zoom, the six fields are (0°, –10.5°), (0°, –12°), (0°, –13.5°), (1.5°, –10.5°), (1.5°, –12°), and (1.5°, –13.5°). For the long-focus zoom, the six fields are (0°, –10.75°), (0°, –12°), (0°, –13.25°), (1.25°, –10.75°), (1.25°, –12°), and (1.25°, –13.25°). The rules to define the feature rays in each field for the two zooms are the same. In this design, the aperture of each field is divided into 16 polar angles with equal intervals; 7 different pupil coordinates are sampled along each radial direction. Each feature ray corresponds to a different pupil coordinate. So, $K = 6 \times 16 \times 7 = 672$ feature rays were used in the surface construction process for each zoom, and in total, $2K = 1344$ feature rays are used. In fact, other reasonable choices for the number of rays can also be employed.

Table 1. Specifications of the Zoom System

Parameter	Short-Focus Zoom	Long-Focus Zoom
FOV	3° × 3°	2.5° × 2.5°
F-number	2	2.4
EFL	180 mm	216 mm
Wavelength	MWIR (3–5 μm)	

During the construction process of each single freeform surface in the conventional CI method, the feature data points on the unknown surface are always calculated in order to redirect all the feature light rays to their ideal image points. This method is effective for traditional freeform system design. However, the zoom system has a special constraint on the EFL. The range of useful solutions, including the power and position of each surface, is limited. As the conventional CI method does not impose a constraint or add pre-knowledge on the distribution of the optical powers on the surfaces in the design process, the obtained solution may not fall into the range of useful solutions. Therefore, the design process will be very difficult and time consuming.

To solve this problem, an approximate equivalent coaxial spherical zoom system can be calculated first as a guide for the off-axis, freeform system design. This coaxial system has the same system specifications as an off-axis, unobscured system. The distances between surfaces in the coaxial system are also the same as those in the unobscured system. Then, the power (or surface curvature) of each surface in the coaxial system can be calculated based on the paraxial theory. In this way, we can obtain a "useful solution" of the surface powers. If we are not considering the aberrations, when the surface powers in the unobscured system are the same as those in the coaxial system, the unobscured system will achieve the desired specifications approximately, and it is enough for the starting point design. In other words, before the direct design process of the unobscured system, the expected optical power of each surface in the system has been

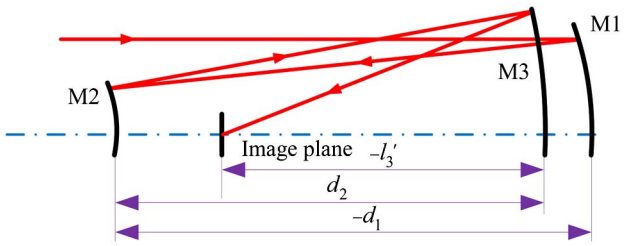

Fig. 3. Scheme of coaxial three-mirror system.

determined approximately. As shown in Fig. 3, based on the paraxial optical theory, for a conventional coaxial three-mirror system, the formulas between the system optical power, surface curvatures, and the distances between surfaces can be written as

$$l_3'\phi = 1 - 2d_1c_1 - 2d_2c_2 + 2d_2c_1 + 4d_1d_2c_1c_2, \quad (1)$$

$$\phi = 2c_3l_3'\phi + 2c_1 - 2c_2 + 4d_1c_1c_2, \quad (2)$$

where ϕ is the optical power of the whole three-mirror system; c_1, c_2, and c_3 are the surface curvatures of the three mirrors; $-d_1$, d_2, and $-l_3'$ are the distances between M1 and M2, M2 and M3, and M3 and the image plane, respectively. The detailed derivations of Eqs. (1) and (2) can be found in Ref. [20].

For a coaxial three-mirror, dual-FOVs, dual-EFLs zoom system, two sets of equations for two different zooms can be put together and the parameters can be solved, as shown in Fig. 4. The equations can be written as follows:

$$l_3'\phi_{z1} = 1 - 2d_{1,z1}c_1 - 2d_{2,z1}c_{2,z1} + 2d_{2,z1}c_1 + 4d_{1,z1}d_{2,z1}c_1c_{2,z1}, \quad (3)$$

$$\phi_{z1} = 2c_3l_3'\phi_{z1} + 2c_1 - 2c_{2,z1} + 4d_{1,z1}c_1c_{2,z1}, \quad (4)$$

$$l_3'\phi_{z2} = 1 - 2d_{1,z2}c_1 - 2d_{2,z2}c_{2,z2} + 2d_{2,z2}c_1 + 4d_{1,z2}d_{2,z2}c_1c_{2,z2}, \quad (5)$$

$$\phi_{z2} = 2c_3l_3'\phi_{z2} + 2c_1 - 2c_{2,z2} + 4d_{1,z2}c_1c_{2,z2}. \quad (6)$$

Here, $\phi_{z1} = -1/180$ mm^{-1} and $\phi_{z2} = -1/216$ mm^{-1} are the optical powers of the whole three-mirror system for the two zooms. They have been determined before the design process; $c_{2,z1}$ and $c_{2,z2}$ are the surface curvatures of M2 for the two zooms; $-d_{1,z1}$, $d_{2,z1}$, $-d_{1,z2}$, $d_{2,z2}$ are the distances between M1 and M2, and M2 and M3 for the two zooms, respectively. c_1, c_2, and l_3' are the same for two zooms. Here, we can make two approximations: (1) the change of the positions of M2 from the first zoom to the second zoom will induce a change of the distance from M1 to M2 as well as the distance from M2 to M3. As the positions of M1 and M3 in the system are approximately symmetric about M2, and the change of M2 position is along the global z direction approximately, here, the changes $|\Delta|$ of two distances are considered to be approximately equal (a very rough approximation, but adequate for a starting design). Considering the sign conventions, we have

$$d_{1,z1} = d_{1,z2} - \Delta \quad \text{and} \quad d_{2,z1} = d_{2,z2} + \Delta. \quad (7)$$

(2) $d_{1,z1}$, $d_{2,z1}$, and l_3' can be obtained from the initial planar system for the short-focus zoom by calculating the distances between the intersections of the chief ray of the central field with the corresponding surfaces. Here, $d_{1,z1} = -366$ mm, $d_{2,z1} = 366$ mm, and $l_3' = -354$ mm. Although it is not very accurate, these values can also be used in Eqs. (3)–(7) to obtain a rough approximation of the surface powers, which is adequate for the starting design. More than one solution for the unknown parameters c_1, c_2, $c_{2,z1}$, $c_{2,z2}$, $d_{1,z2}$, $d_{2,z2}$, and Δ can be generated using Eqs. (3)–(7). Therefore, some boundary conditions are needed to obtain useful solutions. For this design example, the boundary conditions are listed as follows: (a) in order to achieve a compact system, "concave-convex-concave" configuration for M1, M2, and M3 is preferred. So we have $c_1 < 0$, $c_2 < 0$, and $c_3 < 0$. (b) The size of M3 has to be controlled in order to reduce the system volume and eliminate the surface interference with M1. So, the curvature of M2 should not be too large. Here, we constrain $|c_2| < 0.002$. However, using these boundary conditions, there will be still more than one useful solution. If one solution satisfies the boundary conditions and the feasibility of this solution has been checked using optical design software, it can be used for the subsequent design. Proper solutions of c_1, c_3, $c_{2,z1}$, $c_{2,z2}$, and Δ can be obtained; these are -1.443×10^{-4} mm^{-1}, -2.157×10^{-3} mm^{-1}, -1.799×10^{-3} mm^{-1}, -1.493×10^{-3} mm^{-1}, and 69.2368 mm, respectively. Then, the position of the initial planar M2 in the long-focus zoom can be determined and the initial planar system for the long-focus zoom is obtained, as shown in Fig. 2(b).

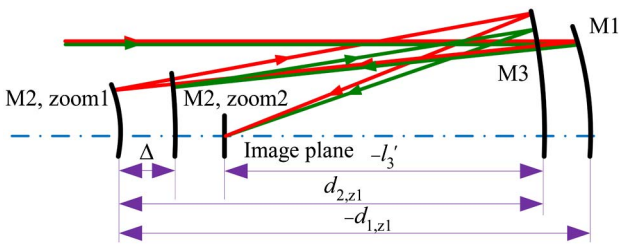

Fig. 4. Scheme of coaxial dual-FOVs three-mirror system.

The next step is to design the freeform surfaces successively with a point-by-point construction process, starting from the initial planes. The feature data points on each unknown surface corresponding to the feature rays are calculated in order to redirect the rays to their desired target points on the image plane. During the design of each surface, the surface power should be approximately consistent with the result obtained from the coaxial design. As a result, when constructing each surface, the target points of the feature rays may be not the ideal image points. The target points should be the ideal intersection

points of the feature rays with the ideal image plane after the current unknown surface has been designed and the corresponding initial plane has been replaced. If we are discussing a coaxial system, the coordinates of these target points with reference to the center of the image plane (the image point of the central field) can be calculated using paraxial theory and geometric relationships. In fact, this is actually the same case for the off-axis system. The only difference is that the center of the image plane is no longer on the axis of rotational symmetry. For the surface that is different for two zooms (M2), the surface in each zoom is constructed individually using only K feature light rays for this zoom. For the surfaces that are the same in the two zooms (M1 and M3), as these surfaces have to control the light rays in both zooms, each surface is constructed using all $2K$ feature rays simultaneously. For one unknown surface $\mathbf{\Omega}$ in the system, the intersection of the first feature ray R_1 and the initial plane is taken as the first data point P_1. It is expected that R_1 can be redirected to the corresponding target point T_1 on the image plane. According to Fermat's principle, the variation of the optical path length between P_1 and T_1 is zero. Therefore, the outgoing direction of R_1 after unknown surface $\mathbf{\Omega}$ as well as the surface normal N_1 at P_1 can be determined. Next, the second data point P_2 can be calculated based on the time-efficient "nearest-ray algorithm" proposed in Ref. [21]. We repeat the above steps until all the feature data points on the unknown surface $\mathbf{\Omega}$ are obtained. The next step is to fit the data points into a freeform surface using a comprehensive fitting method considering both the coordinates and the surface normals of the data points[22]. The corresponding initial plane is then replaced by this new freeform surface. With this method, all the unknown freeform surfaces can be generated successively. Figures 5(a)–5(c) shows the layouts of the systems after constructing freeform M1, M3, and M2, respectively.

However, at this stage, the actual intersection points of the feature light rays with the image plane may have a relatively large deviation from the ideal image points. Therefore, an iteration process can be used to regenerate the freeform surfaces in order to reduce this deviation. The system obtained by the construction process is taken as the new initial system. During the regeneration of each freeform surface, the intersection points of the feature rays with the initial surface are preserved. The target point Ti of each feature ray during the iteration process is determined as

$$T_i = I_{i,\text{ideal}} + \varepsilon(I_{i,\text{ideal}} - I_i^*),$$

where $I_{i,\text{ideal}}$ is the corresponding ideal image point, I_i^* is the actual image point before the current surface is regenerated, $\varepsilon(\varepsilon > 0)$ is the negative feedback coefficient. Here, we choose $\varepsilon = 0.2$. Then, the surface normals of the data points are calculated point by point using the method depicted above. Next, the new freeform surface is obtained with the surface fitting method using these data points and their normals. With this method, the freeform

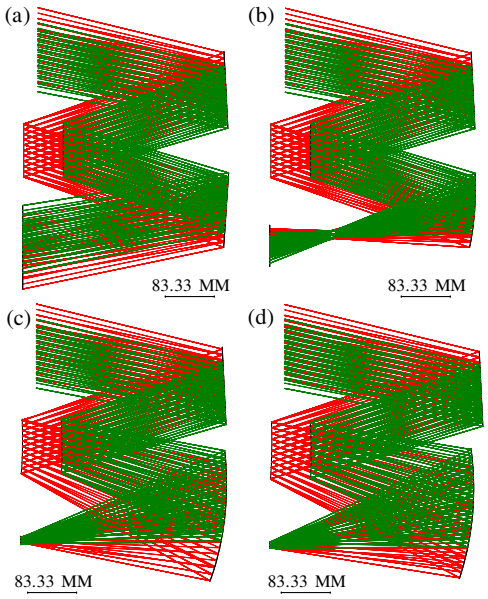

Fig. 5. Layouts of the system after each design stage. (a)–(c) show the layout of system after constructing freeform M1, M3, and M2, respectively. (d) The system after iterations.

surfaces in the system are regenerated successively. This system can be taken as the new initial system for the next iteration. This iteration process can be repeated several times to further decrease the deviation of the rays. Here, the iterations were conducted 70 times. The RMS (root-mean-square) value σ_{RMS} of the distances between the actual image points and the ideal image points for all the feature rays is used to evaluate the effect of the iteration process. The value of σ_{RMS} is decreased by 87.8% after 70 iteration steps. Figure 5(d) shows the system after iterations. The distortion grids of both zooms after iterations are given in Fig. 6. The system after the iteration process can be taken as a good starting point for further optimization.

The optimization was conducted using optical software Code V. The freeform surface type is XY polynomials (up to the fifth order) with a conic base. The final system for after optimization is shown in Fig. 7. The two zooms are plotted together in Fig. 7(a). Figures 7(b) and 7(c) (as well as Figs. 7(d) and 7(e)) show the individual zooms. The switch of the zooms (different FOVs) is achieved by

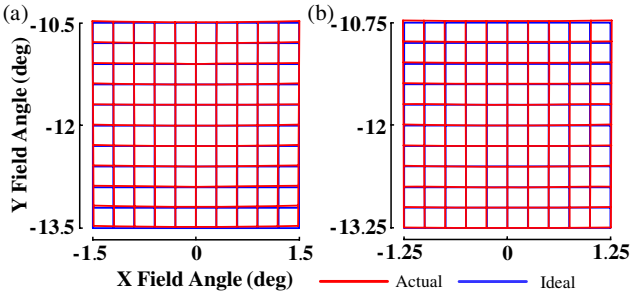

Fig. 6. Distortion grids of both zooms after iterations. (a) The short-focus zoom. (b) The long-focus zoom.

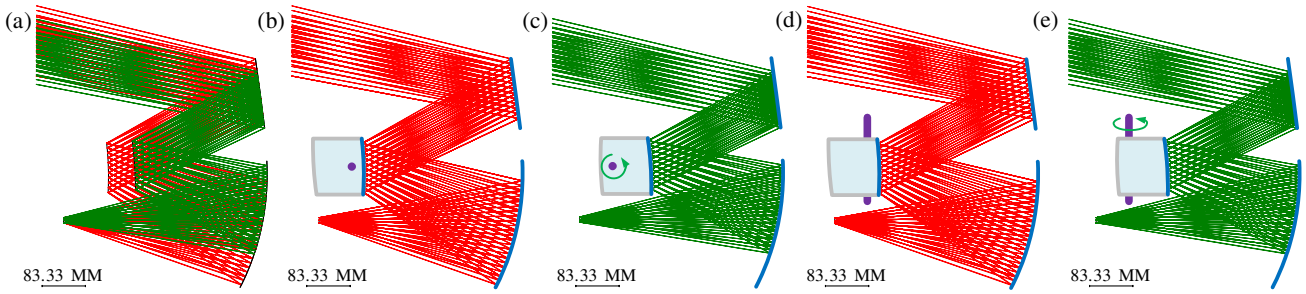

Fig. 7. Layout of the final system for after optimization. (a) The layout of the system with two zooms overlaid in one figure. (b), (c), (d), and (e) show the individual zooms. The switch of the zooms (different FOVs) is achieved by rotating the M2 element along a rotational axis in the x direction (Figs. 7(b) and 7(c)) or the y direction (Figs. 7(d) and 7(e)).

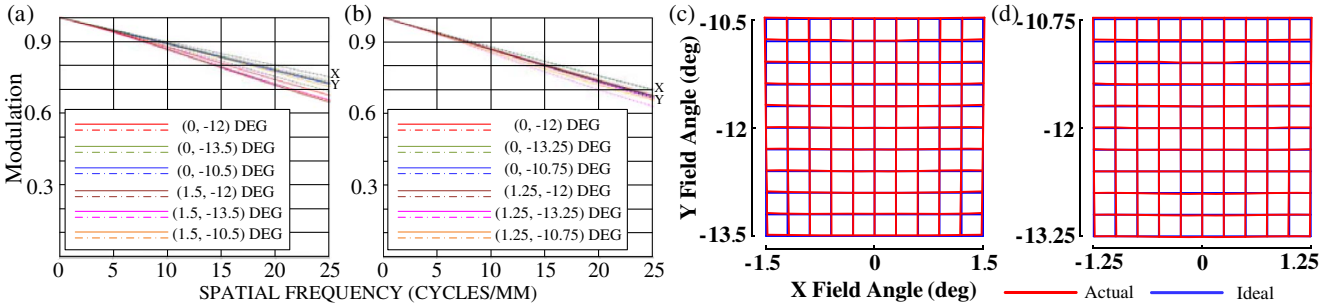

Fig. 8. MTF curves and distortion grids for the two zooms after final optimization. (a) and (c) are for the short-focus zoom. (b) and (d) are for the long-focus zoom.

rotating the M2 element along a rotational axis in the x direction (Figs. 7(b) and 7(c)) or y direction (Figs. 7(d) and 7(e)). The modulation transfer function (MTF) plots of the final system for two zooms are given in Figs. 8(a) and 8(b), which are above 0.62 at 25 lps/mm. The diffraction limits for the two zooms at 25 lps/mm are lower than 0.75. The average RMS wavefront errors of the short-focus and long-focus zooms over the FOV are 0.055λ and 0.03λ, respectively ($\lambda = 4000$ nm). Figures 8(c) and 8(d) shows the distortion grids of both zooms. These results demonstrate that both of the two zooms achieve high performances.

In conclusion, we propose a novel configuration and design method of freeform, dual FOVs, dual EFLs, off-axis, three-mirror zoom system. The design of this kind of system is realized by a point-by-point design approach for the first time. The method is a promising way for the point-by-point design of continuous zoom systems.

References

1. T. Zhang, Y. Wang, and J. Chang, Chin. Opt. Lett. **8**, 701 (2010).
2. J. Chang, Y. Wang, T. Zhang, M. Talha, Z. Wang, and H. Yang, Proc. SPIE **6342**, 63421Q (2006).
3. C. Kuo, C. Lin, and C. Han, Appl. Opt. **49**, 3691 (2002).
4. M. N. Akram and M. H. Asghar, Appl. Opt. **42**, 2312 (2003).
5. X. Wang, M. Jiao, and B. Yang, Proc. SPIE **7383**, 738350 (2009).
6. R. S. Kebo, "Dual band/Dual FOV infrared telescope," U.S. Patent 4,989,962 (1991).
7. J. M. Rodgers, Proc. SPIE **4832**, 33 (2002).
8. X. Hu, W. Wang, Q. Hu, X. Lei, Q. Wei, Y. Liu, and J. Wang, Chin. Opt. Lett. **12**, 072901 (2014).
9. Z. Li, H. Lu, and X. Yuan, Chin. Opt. Lett. **13**, 111101 (2015).
10. G. Xie, J. Chang, J. Zhou, K. Zhang, and X. Wang, Proc. SPIE **9618**, 96180O (2015).
11. F. Fang, X. Zhang, A. Weckenmann, G. Zhang, and C. Evans, CIRP Ann. **62**, 823 (2013).
12. F. Zhang, Chin. Opt. Lett. **13**, S12202 (2015).
13. D. Cheng, Y. Wang, and H. Hua, Proc. SPIE **7849**, 78490Q (2010).
14. R. A. Hicks, Opt. Lett. **33**, 1672 (2008).
15. G. D. Wassermann and E. Wolf, Proc. Phys. Soc. B **62**, 2 (1949).
16. J. C. Miñano, P. Benítez, W. Lin, J. Infante, F. Muñoz, and A. Santamaría, Opt. Express **17**, 24036 (2009).
17. F. Duerr, P. Benítez, J. C. Miñano, Y. Meuret, and H. Thienpont, Opt. Express **20**, 10839 (2012).
18. Y. Nie, H. Thienpont, and F. Duerr, Opt. Express **23**, 34042 (2015).
19. T. Yang, J. Zhu, X. Wu, and G. Jin, Opt. Express **23**, 10233 (2015).
20. J. Zhu, W. Hou, X. Zhang, and G. Jin, J. Opt. **17**, 015605 (2015).
21. T. Yang, J. Zhu, W. Hou, and G. Jin, Opt. Express **22**, 9193 (2014).
22. J. Zhu, X. Wu, T. Yang, and G. Jin, J. Opt. Soc. Am. A **31**, 2401 (2014).